Ionic solutions of 2-dimensional materials

Patrick L. Cullen[1], Kathleen M. Cox[1], Mohammed K. Bin Subhan[1], Loren Picco[2], Oliver D. Payton[2], David J. Buckley[1,3], Thomas S. Miller[3], Stephen A. Hodge[4], Neal T. Skipper[1], Vasiliki Tileli[5] and Christopher A. Howard[1*]

[1]Department of Physics & Astronomy, University College London, London, WC1E 6BT, United Kingdom

[2]Interface Analysis Centre, H. H. Wills Physics Laboratory, University of Bristol, Tyndall Avenue, Bristol, BS8 1TL, United Kingdom

[3]Department of Chemistry, University College London, London, WC1E 6BT, United Kingdom

[4]Cambridge Graphene Centre, 9 JJ Thomson Avenue, Cambridge, CB3 0FA, United Kingdom

[5]Institute of Materials, École polytechnique fédérale de Lausanne, CH-1015 Lausanne, Switzerland

Abstract

Strategies for forming liquid dispersions of nanomaterials typically focus on retarding reaggregation, for example via surface modification, as opposed to promoting the thermodynamically-driven dissolution common for molecule-sized species. Here we demonstrate this true dissolution for a wide range of important 2d nanomaterials by forming layered material salts, which spontaneously dissolve in polar solvents yielding ionic solutions. The benign dissolution advantageously: maintains the morphology of the starting material, is stable against reaggregation, and can achieve solutions containing exclusively individualized monolayers. Importantly, the charge on the anionic nanosheet solutes is reversible, enables targeted deposition over large areas via electroplating and can initiate novel self-assembly upon drying. Our findings thus reveal a unique solution-like behaviour for 2d materials that enables their scalable production and controlled manipulation.

Liquids containing nanomaterials can be used to efficiently print, assemble and embed these materials into functional membranes, films, coatings or composites[1,2,3,4 5,6,7 8,9,10,11,12]. Common routes to forming such liquids involve adding functional groups[3,4], ligands[5,6,7] surfactants[8,9,10] or charge[7,13,14] to the nanomaterials' surfaces in order to decrease inter-particle attraction and thus increase the metastable lifetime of the resulting dispersion. These approaches are traditionally guided by classical models developed for colloidal systems, which balance attractive and repulsive forces between the dispersed species, treating the solvent as a uniform continuum[7,15]. However, the applicability of such models breaks down when the particle size is comparable to that of the ordered solvent layer at its modified surface[15]. In this case, the ordering of the coordinating solvent molecules significantly differs to that in the bulk, and plays a crucial role in determining the dispersion stability[6,15]. Furthermore, associated factors such as hydrogen bonding, steric effects and charge screening, are intrinsically interconnected, invalidating additive and continuum models[15]. Such solvent ordering can be enhanced by charge. For example, densely packed and intricately ordered polar solvent molecules and ionic liquids have been experimentally measured around C_{60} anions[16], and also at charged surfaces respectively[17]. This ordering is congruous to that found in solutions of simple ionic salts, which is understood to underpin their thermodynamic dissolution when the solvent coordinated solute is a more energetically favourable configuration than that of the combined isolated salt and solvent[18].

In this context, 2d nanomaterials offer unique systems in which to examine the crossover from colloidal to solution behaviour. These materials can extend for many

microns in two dimensions while being atomically thin in the third, maximising the surface area in contact with the coordinating solvent molecules. For 2d nanomaterials, achieving efficient liquid-phase delamination from bulk layered 3d analogues is particularly important, since it combines a scalable method for their production with an inbuilt medium for their manipulation into applications[1,2,8,9,10,11]. However, the maximised surface area of the individual layers induces strong van der Waals forces between neighbouring layers that must first be overcome, precluding the spontaneous dissolution of pristine, uncharged layered materials. Current approaches therefore start with significant energy input, for example, by applying shear forces[9], ultrasonication[8,10,11], or chemical reaction[3,19,20,21], to violently break apart the layers. This produces metastable dispersions with an assortment of stack thicknesses and morphologies [3,8,9,10,11,19,20]. Surface modification with functional groups can increase dispersion stability, but degrades the 2d materials' properties[3].

Introducing charges onto the sheets, and concomitant intercalation of solvating exchangeable counterions, can lead to swelling and eventually complete delamination, for some layered materials in water[13,14,22,23]. Examples include the swelling clay minerals, and some expandable layered oxides and hydroxides. In these materials permanent net charges occur naturally on the stoichiometric sheets[13,22,23] or can be incorporated through isomorphic atomic substitution[24,14]. However, for intrinsically uncharged 2d materials, structural isomorphic substitution is not possible, or is detrimental to their underlying properties. In some cases, the layers can be charged reversibly via alkali-metal intercalation and consequent electron transfer and ionization[25]. However, the resultant materials typically react with polar protic solvents, such as water, releasing hydrogen gas between the layers. In some materials

this vigorous reaction can be harnessed to drive exfoliation, but this approach yields meta-stable and heterogeneous dispersions[19,26,27,28]. Some progress has been made via charging then dispersing graphene in aprotic solvents[29,30,31], however, sonication[30] or extensive stirring[29,31] was still used for dispersion. Here we demonstrate that a wide range of reversibly charged 2d materials can *spontaneously dissolve* in polar aprotic solvents without any agitation or chemical reaction, to form ionic solutions.

Results and Discussion

Formation and spontaneous dissolution of layered material salts

Our process starts with intercalated layered material salts that comprise of structurally intact, negatively charged layers separated by arrays of alkali-metal cations (Methods, Fig. 1a, Supplementary Fig. 1). The intercalation process produces a salt in which there is charge transfer from the valance electrons of intercalants to the conduction band of the layered material[25,32,33]. The salts were formed from a wide range of scientifically important layered materials (Supplementary Table 1) including the transition metal dichalcogenides WS_2, $MoSe_2$, TiS_2, MoS_2, the metallic superconductor FeSe, semi-metallic graphite, III-VI and V-VI layered semiconductors Sb_2Te_3, Bi_2Te_3, GaTe and the transition metal oxide V_2O_5. For ion intercalation we used an ammonia-based method, which permits close control over charge stoichiometry and is also performed at low temperature. Both of these facets were found to be essential for avoiding sample decomposition (Methods, Supplementary Information Section 1, Ref 33).

To the layered material salt, an aprotic polar solvent (tetrahydrofuran THF, N-methyl-pyrrolidone NMP, N,N-dimethylformamide DMF) was then carefully added, as

shown for $K_{0.8}Bi_2Te_3$ in Fig. 1c. In contrast to the non-intercalated material (Fig. 1d), the salt gradually dissolves and the increasingly intense Tyndall scattering demonstrates the solute is at least on the scale of tens of nanometres. The resultant solutions are stable in an inert environment. However, upon exposure to air, the solute rapidly precipitates (Fig. 1e, Supplementary Fig. 2). To characterise the spontaneously dissolved species, experiments were performed on an aliquot removed from the uppermost portion of the solution (Fig. 1c), which was dropped and dried onto substrates (Fig. 1f). If a protic solvent such as water is added the salts chemically react as previously shown[19,20,27,28] (Supplementary Information Section 4). The contrasting effect of adding water and DMF is demonstrated for $K_{0.4}MoS_2$ in Supplementary Movie 1.

Morphology of deposited nanosheet solutes

The morphology of the deposited solute was measured with High-Speed Atomic Force Microscopy (HS-AFM) for rapid, height-calibrated data acquisition over large areas (Methods, Ref. 34). Close to the drying rings, agglomerated and overlapping layered structures are found (Supplementary Fig. 3). However, away from these features, high coverage densities of individually isolated nanosheets are deposited. Fig. 2a displays such an area, drop-cast from a $Li^+[TiS_2]^-$/THF solution four weeks after dissolution, and an equivalent dataset for $K^+[Bi_2Te_3]^-$/NMP is shown in Supplementary Fig. 3. Standard line-scan analysis (Fig. 2b,c) was performed for all the deposited nanoparticles in Fig. 2a revealing exclusively plate-like objects of ~1 nm height. However, the image flatness and high density of deposited nanosheets permit a more thorough analysis by obtaining a height histogram of every pixel in the image. The histogram (Fig. 2d) has two distinct peaks: one originates from the mica

substrate, and the other from the deposited nanosheets. These are separated by 1.0 nm, consistent with the observed nanosheets being exclusively TiS_2 monolayers[35]. The roughness, given by the standard deviation derived from a Gaussian fit[36] to the combined pixel heights from all 824 nanosheets, is only ~73 pm, and is therefore comparable to the value of ~47 pm obtained for the atomically flat, naked mica substrate. This contrasts with other liquid exfoliation techniques, where multiple inhomogeneous height contributions are observed across *individual* flakes, attributed to many factors including adsorbed solvent molecules or surfactants[8,9,10,20], functional groups[3], and multilayer fragments[9,11]. By way of contrast, the low total roughness observed here for all the flakes over large areas indicates that the dissolved species are monodisperse, clean and undamaged. It is interesting to note that even at high coverage densities shown in Fig. 2a (Supplementary Fig. 3) the flakes rarely touch. This is consistent with the sheets maintaining electrostatic repulsion upon deposition.

Histograms of the deposited TiS_2 and Bi_2Te_3 nanosheet areas measured from the large area HS-AFM images Fig. 2a and Supplementary Fig. 3 are shown in Fig. 2e. For Bi_2Te_3, we find a Gaussian distribution of deposited sheet areas centred close to the average in-plane lateral crystallite size of the starting powder of 70 ± 20 nm, as determined from XRD (hk0) Bragg peak widths. Bulk TiS_2 had a larger crystallite size of 160 ± 20 nm but the AFM distribution is weighted to lower sheet areas. In this case, smaller flakes have preferentially dissolved, consistent with the expected size dependence of solute diffusion into solution.

To analyse multiple areas on substrates where the nanosheets were more spread out, we identified and extracted step-heights from the raw HS-AFM topographical data via

thousands of automated, independent measurements (Methods and Supplementary Information Section 5). The resulting histograms for 4 different deposited 2d materials are shown in Fig. 2f together with data from a bulk graphite step. In all cases, a single Gaussian distribution centred at heights consistent with the respective monolayers best fits the data.

Crystal structure of nanosheet solutes

The structural integrity of the dissolved nanosheets was investigated with transmission electron microscopy (TEM). Fig. 3a–e shows TEM micrographs of nanosheets and in each case the corresponding selected area diffraction (SAD) patterns exhibit reflections exclusively derived from single-crystal layers of the parent material. Moreover, analogous to bulk single-crystals, the shape of the 2d sheets reflects their underpinning crystal symmetries, in contrast with other brutal exfoliation methods and consistent with gentle dissolution. High Resolution TEM of Bi_2Te_3 (Fig. 3f, zoom in 3g) reveals extended atomic arrays across the hexagonally-shaped nanosheet, consistent with simulations of monolayer units (Supplementary Information Section 8 and Supplementary Fig. 5).

Initial dissolution and electrostatic self-assembly of hexagonal Bi_2Te_3 nanosheets

To better understand the dissolution process, we extracted an aliquot of a $K^+[Bi_2Te_3]^-$ /NMP solution from just above the still-dissolving solute. The resulting deposit was imaged (Fig. 3i) with high-angle annular dark field (HAADF) scanning TEM (STEM) to acquire mass-thickness information across large areas (Methods, Supplementary Information Section 7). In contrast to the dilute solutions (Supplementary Fig. 3) from which only monolayer sheets were found, the nanosheet height, which here is

proportional to the electron scattering intensity, varies from sheet to sheet. It is important to note that the majority of the nanosheets are within themselves of uniform thickness and have sharply defined edges, indicating that they originate from few layer nanosheets, rather than restacked nanosheets. The HAADF intensity histogram (Fig. 3k) reveals four separated, Gaussian-shaped peaks at integer multiples of the first peak above background, attributable to nanosheets of 1-4 monolayer unit thickness (Fig. 3j). The observation of these few layer sheets here indicates the sheets can initially diffuse into solution as few layer stacks, before eventually separating into monolayers.

Figure 3i shows that single layer flakes (top left of composite image) are deposited away from multilayers (bottom right). Whereas the monolayer nanosheets always deposit separately from one another, intriguingly, the thicker sheets ($5 > n > 1$) have self-assembled, preferentially adjoining directly along hexagon edges. Given that no two monolayers touch, we propose that this docking is driven by an electrostatic attraction that is only possible between still-intercalated few layer stacks. For this to occur, the edges of the stacks will connect against one another, offset in the direction normal to the sheets and thereby placing the positive (intercalant) layers of one stack adjacent to the negative (nanosheet) layers of another (Fig 3l). This mechanism naturally yields a variety of shapes such as crosses, lines and rings determined by the crystal symmetry of the 2d units.

Electroplating anionic nanosheet solutes

Finally, to confirm the charging of the dissolved nanosheets, an electric field was applied across two electrodes immersed in a $Li^{+}[MoSe_2]^{-}$/DMF solution, to

electroplate any charged species present (Methods, Fig. 4a). Following deposition, Raman spectra taken from the positive electrode (Figs. 4b, d) exhibit features from intra-layer phonons of $MoSe_2$ Ref. 37 (Fig. 4c) confirming the presence of uncharged deposited $MoSe_2$ nanosheets. Furthermore, an intensity map of the $MoSe_2$ peak at ~241 cm^{-1} (Fig. 4e) shows the nanosheets only plate on to the metallic part of the electrode, i.e. only in the region of the electric field. Identical measurements from the negative electrode showed no $MoSe_2$ features. This experiment confirms that the dissolved nanosheets are negatively charged. It also highlights that once this charge is lost, the sheets do not re-dissolve but, instead, remain adhered to the electrode. Equivalent measurements on a film plated from a 2-year-old $Li^+[MoS_2]^-$/NMP solution (Supplementary Fig. 4) confirm the nanosheets had remained dissolved, charged and undamaged over this time.

Conclusions

The fact that charge is required for the nanosheet dissolution explains why these solutes flocculate upon exposure to air, when charge is depleted by chemical reaction. It is important to note that the demonstrated nanosheet dissolution is not aided by weakening layer-layer attractions upon metal intercalation, which in fact *increases* due to the electrostatic attraction of the anionic sheets and cations[38]. As with simple ionic salts, this electrostatic attraction is then overcome upon solvent introduction due to the energetically favourable solvation of these ions. This dissolution process results in thermodynamically stable solutions, in which the negatively charged solutes are the individualised, undamaged 2d materials that we have observed. Although the size of the dissolved nanosheet is limited by the kinetics of size-dependent diffusion, we have observed dissolved sheets of up to 5 microns for GaTe (Fig. 3e), for which

intercalated macroscopic crystals were used rather than fine powders. Importantly, we have shown that the anionic nature of the dissolved 2d materials permits their targeted large-scale deposition via electroplating and leads to novel electrostatic self-tiling, providing new routes for their manipulation into technological applications.

Methods

Preparation of layered material salts

Layered materials (structure and properties Supplementary Table 1) were first heated at elevated temperatures (Supplementary Table 2) under dynamic vacuum < 10^{-6} mbar for at least 24 hours, to remove adsorbed impurities. The materials were then loaded with a predetermined amount of alkali metal (Supplementary Table 2) into a quartz tube and attached to a clean, pre-baked, leak-tight, custom gas-handling manifold. The tube was cooled to -63 °C and high-purity ammonia gas, which had been further cleaned by multiple sodium washes, was condensed. Following intercalation, the ammonia was slowly removed by cryopumping at low temperatures. The resulting salt was then further dried by vacuum treatment, before being removed to a high purity argon glovebox (O_2, H_2O <0.1 ppm). Further discussion of the intercalation process is given in Supplementary Information Section 1.

Dissolution of layered salts

Excess anhydrous aprotic solvents, which had been further dried with zeolite crystals, were added to the layered salts. Care was taken not to disturb the salt upon solvent addition, and the salt was left to dissolve, without agitation, for at least 2 weeks prior to experiments. To examine the solutes, aliquots were taken from the uppermost portion of the resulting solution as shown in Fig. 1c to minimise the unintentional

extraction of still dissolving salt when examining the solutions. Further details are given in Supplementary Information Section 3.

X-ray Diffraction (XRD)

Salts were placed in capillaries and sealed with wax within the glovebox. Diffraction patterns were measured in transmission geometry on a Stoe Stadi-P (Cu) Capillary Power XRD with Pure Kα1 radiation. Diffraction patterns are presented in Supplementary Fig. 1 and discussed in Supplementary Information Section 2.

High-Speed Atomic Force Microscopy (HS-AFM)

Topography measurements were undertaken on a custom-built contact-mode HS-AFM[34,39]. HS-AFM permits rapid data acquisition over large areas with sub-nanometre topological height accuracy minimising many of the drift-effects that typically plague conventional AFMs[40]. HS-AFM samples were prepared by dropping the nanosheet solutions onto freshly cleaved mica substrates in the glovebox, and the drying of the solvent took place under vacuum at $< 10^{-6}$ mbar for 1 week.

The HS-AFM used in this study is equipped with a Laser Doppler Vibrometer (LDV) (Polytec CLV-2534) for a direct measurement of the sample's topography under the silicon nitride tip of the microcantilever (Bruker MSNL, tip radius 2 nm nominal, 12 nm max). By measuring the cantilever displacement, as opposed to optical beam deflection, the HS-AFM is immune to many of the sources of noise found in conventional AFMs[39,40]. The displacement signal from the LDV is used directly to map sample topography at 2 megapixels per second. A custom piezo flexure stage oscillates the sample under the microcantilever in a sinusoidal raster scan pattern

providing a 16 μm^2 imaging window with 2 nm pixel size at two frames per second. The imaging window is automatically panned across the sample using closed-loop stiction drives (SmarAct, Germany). The method followed for determining nanosheet height is given in Supplementary Information Section 5.

Electron Microscopy

TEM and STEM were performed on a Jeol JEM 2100 equipped with a LaB_6 source operated at 200 kV. The atomically resolved Bi_2Te_3 micrographs were acquired using an FEI Titan 60–300 operated at 80 kV, equipped with a high-brightness electron gun and a Cs and Cc corrector at the image plane. The corrector was tuned for minimum Cs (close to zero) and images were taken with the specimen very close to focus. It is noted that structural damage caused by the intense electron beam irradiation in transmission mode was a limiting factor, particularly for high-resolution work. In low-resolution however, the selected area diffraction patterns confirm the intact crystal structure of the 2d sheets. The acquisition and analysis of STEM data are described in Supplementary Information Section 7.

Electroplating

An electric field of ~1 Vcm^{-1} was applied across two platinum coated oxidised silicon electrodes, to a solution of dissolved nanosheets, for 24 hours in a custom-built cell inside a high purity glovebox. Following plating, the electrodes were dried overnight under a vacuum of < 10^{-6} mbar at ~100 ºC for the $MoSe_2$ film and at room temperature for the MoS_2 film.

Raman spectroscopy

Raman spectra were taken using a Renishaw In-Via microscope with a 514.5 nm laser through a x50 objective, giving a spot size of ~3 μm. Spectra were taken from a grid of positions on each sample and the peaks fitted with Lorenztian line-shapes (Supplementary Information Section 6)

END NOTES

Supplementary Information is available in the online version of the paper.

Acknowledgements

This publication was funded, in part, by the Engineering & Physical Sciences Research Council (EPSRC). L.P. & O.D.P. thank the Royal Academy of Engineering for funding the development of the HS-AFM and the NSQI Low Noise Lab for hosting the HS-AFM. We thank Martial Duchamp for his valuable assistance with the "PICO" TEM at the Ernst-Ruska Research Centre. The authors are grateful to Milo Shaffer & Paul McMillan for helpful and supportive discussions.

Author Information

Reprints and permissions information is available at XXX. The authors declare no competing financial interests. Correspondence and requests for materials should be addressed to C.A.H. (c.howard@ucl.ac.uk)

[1] Nicolosi, V., Chowalla, M., Kanatzidis, M. G., Strano, M. S. & Coleman, J. N. Liquid exfoliation of layered materials. *Science* **340**, 1226419 (2013).
[2] Ferrari, A. C. *et al.* Science and technology roadmap for graphene, related two-dimensional crystals, and hybrid systems. *Nanoscale* **7(11)**, 4598-4810 (2015).

[3] Stankovich, S. *et al.* Synthesis of graphene-based nanosheets via chemical reduction of exfoliated graphite oxide. *Carbon* **45(7)**, 1558-1565 (2007).
[4] Hummelen, J. C. *et al.* Preparation and characterization of fulleroid and methanofullerene derivatives. *J. Org. Chem.* **60(3),** 532-538 (1995).
[5] Sperling, R. A. & Parak, W. J. Surface modification, functionalization and bioconjugation of colloidal inorganic nanoparticles. *Phil. Trans. R. Soc. A* **368**, 1333-1383 (2010).
[6] Zobel, M., Neder, R. B. & Kimber, S. A. Universal solvent restructuring induced by colloidal nanoparticles. *Science* **347**, 292-294 (2015).
[7] Boles, M. A., Ling, D., Hyeon, T. & Talapin, D. V. The surface science of nanocrystals. *Nat. Mat.* **15** 141-153 (2016).
[8] Lotya, M. *et al.* Liquid phase production of graphene by exfoliation of graphite in surfactant/water solutions. *J. Am. Chem. Soc.* **131(10)**, 3611-3620 (2009).
[9] Paton, K. R. *et al.* Scalable production of large quantities of defect-free few-layer graphene by shear exfoliation in liquids. *Nature Mater.* **13(6)**, 624-630 (2014).
[10] Shih, C. J. *et al.* Bi-and trilayer graphene solutions. *Nature Nanotech.* **6(7)**, 439-445 (2011).
[11] Coleman, J. N. *et al.* Two-dimensional nanosheets produced by liquid exfoliation of layered materials. *Science* **331**, 568-571 (2011).
[12] Huo, C., Yan, Z., Song, X. & Zeng, H. 2D materials via liquid exfoliation: a review on fabrication and applications. *Sci. Bull.* **60** 1994-2008 (2015)
[13] Ma, R. & Sasaki, T. Two-dimensional oxide and hydroxide nanosheets: controllable high-quality exfoliation, molecular assembly, and exploration of functionality. *Acc. Chem. Res.* **48**, 136−143 (2015).
[14] Stöter, M., Rosenfeldt, S. & Breu, J. Tunable exfoliation of synthetic clays. *Annu. Rev. Mater. Res.* **45**,129–51 (2015).
[15] Silvera Batista, C. A., Larson, R. G. & Kotov, N. A. Nonadditivity of nanoparticle interactions. *Science* **350,** 6257 (2015).
[16] Howard, C. A., Thompson, H., Wasse, J. C. & Skipper, N. T. Formation of giant solvation shells around fulleride anions in liquid ammonia. *J. Am. Chem. Soc.* **126(41)**, 13228-13229 (2004).
[17] Mezger, M. *et al.* Molecular layering of fluorinated ionic liquids at a charged sapphire (0001) surface. *Science* **322**(5900), 424-428. (2008).
[18] Burgess, J. *Ions in solution: basic principles of chemical interactions* (Horwood, Chichester, ed. 2, 1999)
[19] Joensen, P., Frindt, R. F. & Morrison, S. R. Single-layer MoS_2. *Mater. Res. Bull.* **21(4)**, 457-461 (1986).
[20] Eda, G. *et al.* Photoluminescence from chemically exfoliated MoS_2. *Nano Lett.* **11(12)**, 5111-5116 (2011).
[21] Lu, X. *et al.* Preparation of MoO_3 QDs through combining intercalation and thermal exfoliation. J. Mat. Chem. C, **4**, 6720 (2016).
[22] Schaak, R. E. & Mallouk, T.E., Prying Apart Ruddlesden-Popper Phases: Exfoliation into Sheets and Nanotubes for Assembly of Perovskite Thin Films. *Chem. Mater.* **12**, 3427-3434 (2000).
[23] Sasaki,T., Watanabe, M., Hashizume, H., Yamada, H., & Nakazawa, H. Macromolecule-like aspects for a colloidal suspension of an exfoliated titanate. Pairwise association of nanosheets and dynamic reassembling process initiated from it. *J. Am. Chem. Soc.* **118**, 8329-8335 (1996).

[24] Sposito, G., Skipper, N. T., Sutton, R., Park, S. H., Soper, A. K., & Greathouse, J. A. Surface geochemistry of the clay minerals. *Proceedings of the National Academy of Sciences*, *96*(7), 3358-3364 (1999).
[25] Dresselhaus, M. S. & Dresselhaus, G. Intercalation compounds of graphite. *Advances in Physics* **51**:1, 1-186 (2002).
[26] Fan, X. *et al.* Controlled exfoliation of MoS_2 crystals into trilayer nanosheets *J. Am. Chem. Soc.* **138(15)** 5143–5149 (2016).
[27] Ding, Z., Viculis, L., Nakawatase, J. & Kaner, R.B. Intercalation and Solution Processing of Bismuth Telluride and Bismuth Selenide. *Adv. Mater*. **13 (11)**, 797-800 (2001).
[28] Zeng, Z. *et al.* Single layer semiconducting nanosheets: high-yield preparation and device fabrication. *Angew. Chem. Int. Ed*., **50** (47) 11093–11097 (2011).
[29] Vallés, C. *et al.* Solutions of negatively charged graphene sheets and ribbons. *J. Am. Chem. Soc.* **130(47)**, 15802-15804 (2008).
[30] Milner, E. M. *et al.* Structure and morphology of charged graphene platelets in solution by small-angle neutron scattering. *J. Am. Chem. Soc.* **134(20)**, 8302-8305 (2012).
[31] Huang, K., *et al.* Single layer nano graphene platelets derived from graphite nanofibres. *Nanoscale* **8(16)**, 8810 (2016).
[32] Pan, Z. -H., *et al.* Electronic structure of superconducting KC_8 and nonsuperconducting LiC_6 graphite intercalation compounds: evidence for a graphene-sheet-driven superconducting state. *Phys. Rev. Lett.* **106**, 187002 (2011).
[33] Somoano, R. B., Hadek, V. & Rembaum, A. Alkali metal intercalates of molybdenum disulfide. *J. Chem. Phys.* **58(2)**, 697-701 (1973).
[34] Picco, L. M. *et al.*, Breaking the speed limit with atomic force microscopy. *Nanotechnology* **18**(4), 044030 (2006).
[35] Zeng, Z., Tan, C., Huang, X., Bao, S., & Zhang, H. Growth of noble metal nanoparticles on single-layer TiS_2 and TaS_2 nanosheets for hydrogen evolution reaction. *Energy Environ. Sci*. **7**, 797 (2014)
[36] Lui, C. H., Liu, L., Mak, K. F., Flynn, G. W. & Heinz, T. F. Ultraflat graphene. *Nature* **462**, 339-341 (2009).
[37] Tonndorf, P. *et al.* Photoluminescence emission and Raman response of monolayer MoS_2, $MoSe_2$, and WSe_2. *Opt. Express* **21(4)**, 4908-4916 (2013).
[38] Yoon, G. *et al.* Factors affecting the exfoliation of graphite intercalation compounds for graphene synthesis. *Chem. Mater.* **27(6)**, 2067-2073 (2015).
[39] Payton, O. D. *et al.* Experimental observation of contact mode cantilever dynamics with nanosecond resolution. *Rev. Sci. Instrum.* **82(4)**, 043704 (2011).
[40] Kodera, N., Yamamoto, D., Ishikawa, R. & Ando, T. Video imaging of walking myosin V by high-speed atomic force microscopy. *Nature* **468**, 72-76 (2010).

Figures

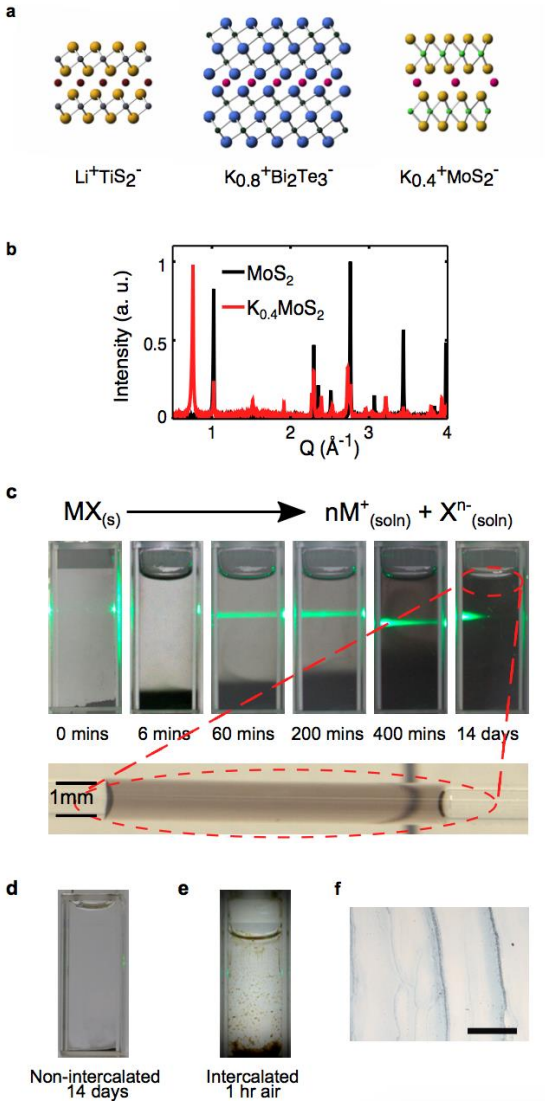

Figure 1 | Structure, dissolution, and deposition of layered material salts. a, The layered material salts: $LiTiS_2$, $K_{0.8}Bi_2Te_3$ and $K_{0.4}MoS_2$, alkali metal ions (Li turquoise, K purple) are situated between intact, negatively charged monolayer units of the parent layered material. **b**, X-ray diffraction patterns of MoS_2 pre- and post-intercalation with potassium. **c**, Dissolution time sequence for the aprotic organic solvent DMF added to the layered salt $K_{0.8}Bi_2Te_3$. As the salt gradually dissolves, concomitant increasing Tyndall scattering (green laser beam) indicates the solutes are nanoparticles. A photograph of the solution in through a 1 mm diameter pipette shows no visible particulates. **d**, DMF added to non-intercalated Bi_2Te_3 after two weeks showing no Tyndall scattering. **e**, The solution shown in **c** following 1 hour exposure to air. **f**, Nanoparticle solute deposits on mica (scalebar 200 μm).

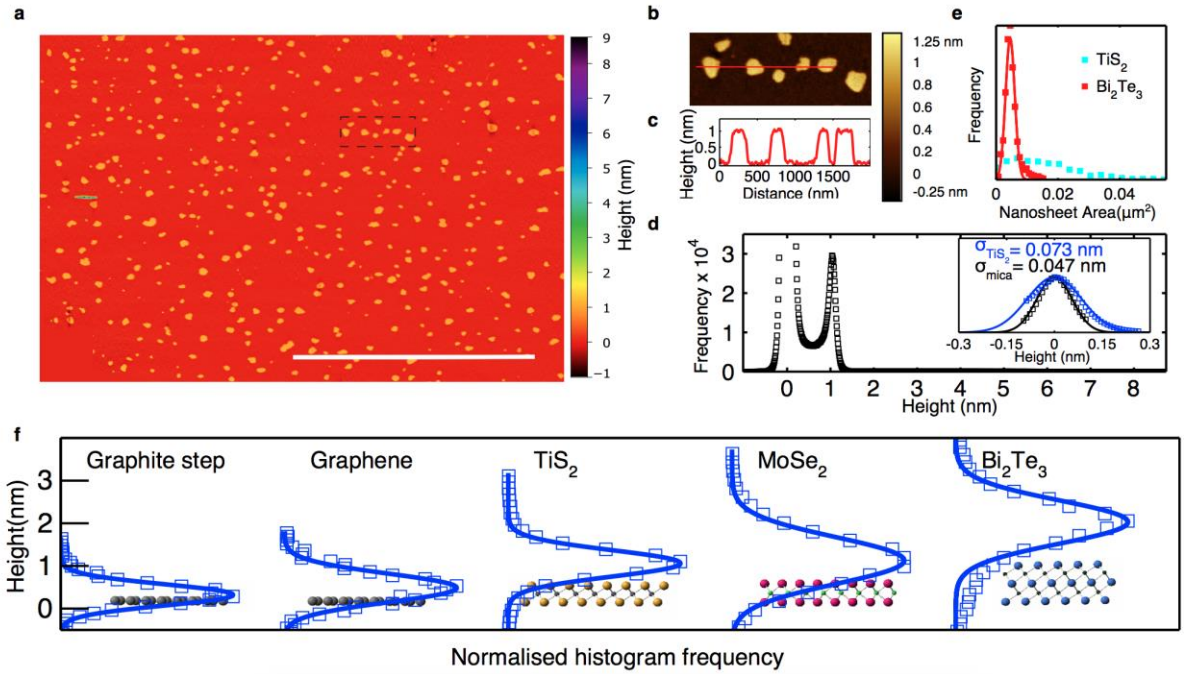

Figure 2 | The morphology of dissolved nanosheets. **a**, Composite HS-AFM image of solution deposited TiS_2 nanosheets on a mica substrate, scalebar 5 μm. **b**, Zoom-in corresponding to the dashed rectangle, and associated linecut **c** taken from the red line. **d**, Height histogram of all ~1.9 x 10^7 pixels from **a** showing a peak corresponding to all of the deposited nanosheets 1.0 nm above the mica substrate peak at 0 nm. Inset, comparison of data (squares) and Gaussian fits (solid lines) from histogram peaks from the mica (black) and the TiS_2 nanosheets (blue). **e**, Deposited TiS_2 nanosheet area histogram from **a** (cyan squares), and Bi_2Te_3 (from Supplementary Fig. 3) (red squares), the Bi_2Te_3 histogram data is fitted with a Gaussian distribution (red curve). **f** Normalised histograms of automatically detected and measured step heights from: a step on a HOPG graphite surface (5,059), graphene (1,583), TiS_2 (14,439) and $MoSe_2$ (11,415), deposited from THF solution, and Bi_2Te_3 (7,441) deposited from NMP. The number in bracket corresponds to the number of independent step-height measurements used for the histograms in **f**. On the same figure are approximately scaled representations showing monolayer units of the corresponding layered materials.

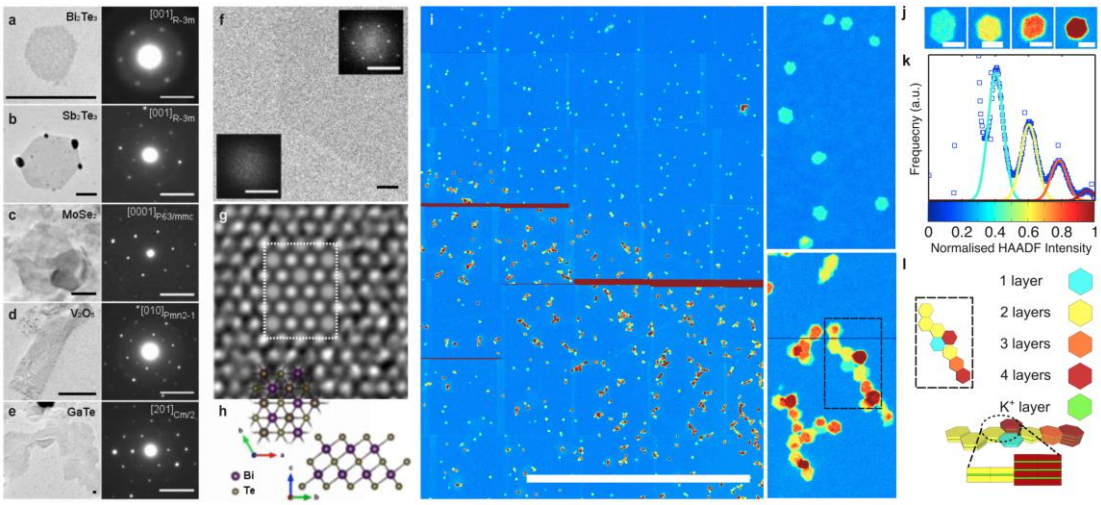

Figure 3 | Structure and self-assembly of dissolved nanosheets. a-e, TEM micrographs of Bi_2Te_3, Sb_2Te_3, $MoSe_2$, V_2O_5 and GaTe nanosheets, alongside their corresponding SAD patterns marked with in-plane orientation and space groups for each structure (image scalebars are 100 nm and SAD scalebars are 5 nm^{-1}). **f**, shows the 120° facet of a Bi_2Te_3 single layer (scalebar 10 nm) which is confirmed with Fast Fourier Transform (FFT) data (scalebars 5 nm^{-1}) from inside the hexagon and the carbon support, and **g** depicts its atomic structure overlaid with image simulation and crystallographic models **h**. **i**, Composite (stitched) HAADF image showing Bi_2Te_3 nanosheets deposited from concentrated solution (scalebar 10 μm) alongside zooms showing isolated and adjoined hexagonal nanosheets. **k**, HAADF Scattering intensity histogram from **i** and fit from 4 individual Gaussian distributions corresponding to nanosheets of 1 to 4 layer thickness shown individually in **j** (scalebar 0.1 μm). **l**, Proposed model for electrostatic self-tiling in which neighboring nanosheets are attracted electrostatically, along their vertically offset edges upon drying. In this model the edges are offset in the plane normal to the face of the sheet to place positive layers adjacent to negative ones.

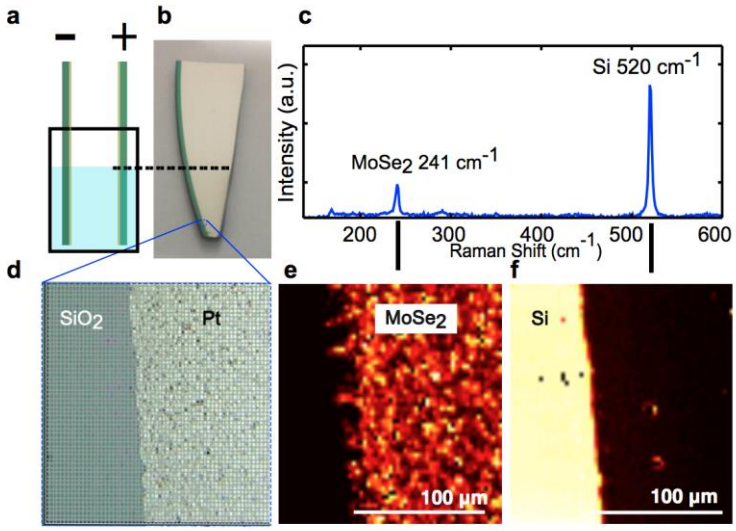

Figure 4 | Electroplating a nanosheet solution. a, Schematic of electroplating set up. **b**, Photograph of the positive electrode following electrodeposition. **c**, Raman spectrum from the plated region on the positive electrode, showing features from intra-layer phonons of deposited $MoSe_2$ nanosheets and the substrate below. **d**, Optical micrograph showing grid over which Raman spectra were taken. **e**,**f**, Raman intensity maps of fitted $MoSe_2$ peak at ~241 cm^{-1} and fitted silicon peak at ~520 cm^{-1} respectively.

Supplementary Information: Ionic solutions of 2-dimensional materials

Patrick L. Cullen[1], Kathleen M. Cox[1], Mohammed K. Bin Subhan[1], Loren Picco[3], Oliver D. Payton[3], David J. Buckley[1,2], Thomas S. Miller[2], Stephen A. Hodge[4], Neal T. Skipper[1], Vasiliki Tileli[5] and Christopher A. Howard[1*]

[1]Department of Physics & Astronomy, University College London, London, WC1E 6BT, United Kingdom
[2]Department of Chemistry, University College London, London, WC1E 6BT, United Kingdom
[3]Interface Analysis Centre, H. H. Wills Physics Laboratory, University of Bristol, Tyndall Avenue, Bristol, BS8 1TL, United Kingdom
[4]Cambridge Graphene Centre, 9 JJ Thomson Avenue, Cambridge, CB3 0FA, United Kingdom
[5]Institute of Materials, École polytechnique fédérale de Lausanne, CH-1015 Lausanne, Switzerland

1. **Preparation of layered material salts**
2. **X-ray diffraction (XRD) of layered material salts**
3. **Dissolution of layered salts**
4. **Demonstrating the difference between spontaneous dissolution and chemical exfoliation**
5. **Determination of nanosheet height using HSAFM**
6. **Raman mapping experiments**
7. **Acquisition and analysis of STEM data**
8. **HRTEM simulations of Bi_2Te_3 nanosheets**
9. **Caption for Supplementary Movie 1**

Supplementary Figure 1 | XRD of layered material salts
Supplementary Figure 2 | Solutions of layered material salts
Supplementary Figure 3 | HS-AFM of solution deposited nanosheets
Supplementary Figure 4 | Stability and electroplating of a 2 year old MoS_2 nanosheet solution
Supplementary Figure 5 | Experimental data and image calculations of high resolution TEM of Bi_2Te_3 (001)

1. Preparation of layered material salts

The outgassed layered material was loaded in a quartz tube with a predetermined amount of alkali metal, and ammonia condensed at -60°C (methods, main text). The amount of ammonia added to the metal was determined so that the initial metal-ammonia solution was at a concentration of less than 2 mole-per cent metal, i.e. in the dilute regime, containing solvent-isolated electrons that give the solution its characteristic blue colour[41]. The layered material was left in the metal-ammonia solution for 1-4 days until the colour completely disappeared. This indicates the electrons had transferred from solution onto the sheets of the layered material. The choice of metal:layered material stoichiometry was important. In particular, with an excess of alkali metal, solvated electrons that remained after intercalation could decompose the intercalated salt. This was often visually apparent from a colour change of the ammonia arising from dissolved reduced ionic species, and further evident from impurity phases visible in X-Ray Diffraction (XRD) or Transmission Electron Microscopy (TEM). Therefore, where the composition of the target material was known, less alkali metal than the full stoichiometric ratios was added. The penalty for this was a portion of phase pure non-intercalated material (Supplementary Fig. 1), rather than the production of potentially soluble decomposition products. Decomposition could also occur within our process with: modest increases in temperatures, any leaks in the gas manifold, or residual impurities in the apparatus or starting materials. Decomposition of the metal-ammonia solution is also detrimental to the process and leads to production of hydrogen gas, which was monitored via measuring an increase in residual gas pressure following ammonia removal. However in the singular case of FeSe some of the ammonia decomposes as part of the process and intercalates along with the metal, as previously shown[42].

Once intercalation was complete, ammonia was removed by cryopumping while the sample remained at low temperature. Cryopumping too fast or at higher temperatures could also cause decomposition and/or deintercalation. Choice of alkali metal was guided by literature values of the stoichiometries of known salts, and our own investigations of combinations that produced salts reliably without decomposition products. For MoS_2 we used both K and Li as intercalants in separate experiments, but no significant difference in the resultant solutions themselves, or in the character of the dissolved nanosheets was observed. The ability to continuously tune the intercalant concentration in a layered material is rare, but some discrete variations in charge stoichiometry are possible in some materials, for example graphite[43] (although this is often accompanied by a stage change – where stage refers to the number of graphene layers between each intercalant layer) or MoS_2, (although this can also result in a structural change of the MoS_2 layers from 2H to 1T polymorph)[44]. However, optimisation of the stoichiometry and choice of metal species for individual materials is ongoing.

It is worth noting that the intercalation process described here is driven by the initial reduction of the layers by the solvated electrons. This means 2d materials with large

bandgaps, such as hexagonal boron nitride, cannot be intercalated via this method. However, it should also be noted that this ammonia-based method can be applied to materials for which intercalation without degradation is difficult via vapour transport[45] or electrochemistry, e.g Bi_2Te_3 (Ref 46). Importantly, the ammonia-based intercalation method is intrinsically scalable.

2. X-ray diffraction (XRD) of layered material salts

The diffraction patterns of the layered material salts are shown in Supplementary Fig. 1. The peaks corresponding to non-intercalated layered material are indicated in the figure by an asterisk. In all cases where the structure has been previously reported, i.e. for $Li_{0.6}(NH_2)_{0.2}(NH_3)_{0.8}Fe_2Se_2$ (Ref 42) $K_{0.4}MoS_2$ (Ref 45), $LiTiS_2$, $LiWS_2$, $LiMoSe_2$ (Ref 47), the diffraction patterns of the intercalated salts match literature values. For $K_{0.8}Bi_2Te_3$ and $LiSb_2Te_3$ we report the first diffraction data, to the best of our knowledge. In these cases, the diffraction patterns showed only very small changes from the parent material upon intercalation, consistent with literature data of other intercalation compounds of these and similar materials [48, 49]. High-resolution diffraction measurements are currently being undertaken to solve the structure of these materials and will be reported elsewhere. For $KC_{24}(NH_3)_{1.3}$ our powder diffraction pattern matches published data for 00l reflections of a stage one graphite intercalation compound [50]. The other peaks derive from a hexagonal in-plane superlattice attributable to the intercalated species.

3. Dissolution of layered salts

For this work, we chose three archetypical aprotic polar solvents: tetrahydrofuran THF, boiling point (b.p.) 66 °C, room temperature dielectric constant (ε_r) 7.58, *N*,*N* -dimethylformamide (DMF) b.p. 152 °C, ε_r 36.7, and N-methyl-2-pyrrolidone (NMP) b.p. 202 °C, ε_r 32.2. We found different solvents suited different experimental techniques. For example, NMP was difficult to remove from mica for AFM but was found to protect the nanosheets from electron beam damage during TEM. Interestingly, NMP solutions typically took longer to flocculate when exposed to air, consistent with this solvent's ability to maintain dispersions of uncharged nanoparticles for relatively long periods of time once isolated[51]. The dissolution of the nanosheets into the solvent depends, among other factors, on their size in the starting material. Moreover, the equilibration times are long (of the order of months) and highly material dependent. Therefore establishing properties such as the saturation concentrations of the solutions for each material/solvent under the constraint of spontaneous conditions is not feasible. In this context, the thermodynamically-driven dissolution process observed here implies a yield of dissolution of nanosheets into solution of 100%, assuming a perfect crystal is left long enough in dilute conditions. However, the overall process-yield will also depend on the extent to which the material is intercalated, and the residual amount of impurities in the solvent/container that may oxidise the salt. The practicality of the slow initial dissolution time is mitigated by the indefinite shelf life afforded by thermodynamic stability of the

solutions, and the fact that no post exfoliation (ultra)centrifugation steps are needed. Ultracentrifugation is necessary to remove undesirable stirred up material from violent liquid exfoliation processes, and this process is difficult to scale industrially[51,52,53].

4. Demonstrating the difference between spontaneous dissolution and chemical exfoliation

If a protic solvent such as water is added to the intercalated layered material salt a chemical reaction typically occurs evolving hydrogen gas as previously shown[54]. This difference is important to highlight because, for some materials, the evolution of hydrogen gas between the layers can be harnessed for layer exfoliation. This process is often known as "chemical exfoliation", it is typically accompanied by (ultra)sonication, and centrifugation is necessary to remove large aggregates and reduce the number of multilayer nanosheets. The nanosheets produced this way range in layer number, depending on the intercalant and layered material[52,53]. However, in general, the monolayer fraction is much larger than liquid-based exfoliation methods that do not start with intercalation compounds[53].

The difference in behaviour between adding a protic and an aprotic solvent to the same amount of $K_{0.4}MoS_2$ is demonstrated in Supplementary Movie 1. This movie shows in real time the first 28 seconds following the addition of dry DMF (left) and DI water (right) being added to equal amounts of $K_{0.4}MoS_2$ powder in quartz cells (path length 0.4 mm). Whilst no visible chemical reaction occurs upon the addition of aprotic DMF, the water reacts with the $K_{0.4}MoS_2$ evolving hydrogen gas exfoliating the sheets and forming a dispersion. After 20 days, photographs of the same samples are shown. The quartz cells have been rotated 90˚ to view through the longer path length of each cell (1 mm) to highlight the contrast between the samples. Some of the $K_{0.4}MoS_2$ has now dissolved in the aprotic DMF to form a brown/yellow solution, while the $K_{0.4}MoS_2$ dispersion in water has flocculated.

Chemical exfoliation is most widely studied for MoS_2. For this material the process results in the partial or complete phase transformation from the 2H-MoS_2 phase of the starting material, to the meta-stable, 1T-MoS_2 polymorph[53,55]. The 2H-MoS_2 phase can be recovered by high temperature annealing[55].

In the dissolution process reported here, there was no evidence for 1T-MoS_2 among deposited nanosheets. Raman spectra for 1T-MoS_2 and 2H-MoS_2 have clear differences in the same spectral region[53,55]. Supplementary Fig. 4 shows Raman spectra and maps from 649 spectra over a 10 μm x 66 μm grid on a MoS_2 thin film deposited via electroplating 2 years after the solution was produced. All spectra show exclusively 2H-MoS_2 related peaks. Furthermore, there is no discernible increase in peak-width from that of the starting material, despite the long time the charged sheets were in solution. Previously, an increase in (2H-MoS_2) Raman peak widths for chemically exfoliated nanosheets, recovered following annealing have been attributed

to thickness inhomogeneities, increase in defects and the small size of the deposited flakes[55].

5. Determination of nanosheet height using High Speed AFM

Two methods were used to measure the height of the nanosheets, depending on the amount of residual solvent on the substrate and coverage density of the deposited flakes. If the sample is locally disperse and solvent free each image can be reliably flattened and the height and roughness of both the mica background and the nanosheet determined from a height histogram of all the pixels in the image, as shown in Fig. 2. Once flattened multiple images may be stitched together using the sensor values from the SmarAct positioning stages as initial estimates for the approximate location of each frame in the large composite image.

If impurities or solvent remained on the sample surface, the flattening of each image induces greater uncertainty and the resulting accuracy of the height histogram is adversely affected[56,57,58]. Therefore, an image analysis algorithm was implemented to perform appropriate thresholding to select nanosheet edges far from any contaminants that might add to background height. Once identified, each step edge was then measured by performing a linear least squares fit to the mica substrate directly preceding the step and then extrapolating this fit to a point at least 6 nm (3 pixels) beyond the top edge of the nanosheet (as detected using the second derivative of the topography). This extrapolation prevents any edge effects, such as increased roughness or contaminants, from unduly influencing the step height measurement. This automated method enables the rapid winnowing of the whole dataset to locate isolated nanosheets and permitted automated measurement of thousands of step heights per sample. Although it is well known that step height measurements are highly sensitive to uncertainty (noise) in the measurement of the baseline of the background (mica) it is important to note that such uncertainty is random, not systematic. As such, it broadens the Gaussian distribution of step heights measured but does not affect the mean of the distribution. Therefore, provided that a suitably large number of step height measurements are performed, it is possible to fit a Gaussian to the data and recover an average height of the nanosheets independent of signal-to-noise absolute values. The height analysis of the layer step-height on a freshly-cleaved bulk graphite surface (Fig. 2f) confirms the soundness of the analysis and the non-limiting statistical noise of the measurements is estimated by the width of its height distribution (shown in Fig. 2f).

6. Raman mapping experiments

For the electrode plated from a $Li^+[MoSe_2]^-$/DMF solution shown in Fig.4, Raman spectra were taken from 3447 positions across a 168 μm x 180 μm grid (Fig. 4d). Each was fitted with Lorenztian line-shapes in the window for the $MoSe_2$ peak at 240.9 cm^{-1} and silicon peak at ~520 cm^{-1}. In the absence of peaks, the intensity was set to zero. A similar process was performed on an electrode plated from a 2-year-old $Li^+[MoS_2]^-$ /NMP solution. In this case, two Lorenztian peaks were fitted to the

spectra at ~383 and ~406 cm^{-1}, on 649 points across a 10 μm x 66 μm grid, all of which exhibited these two peaks. The resulting intensity and position maps from the fitted peaks are shown in Supplementary Fig. 4.

7. Acquisition and analysis of STEM data

The stitched STEM image was acquired in a snake-like manner by multiple (7x7) high angle annular dark field (HAADF) images (1024x1024 pixel size). A representative segment of it is shown in Fig. 3i. The image intensity (I) in HAADF imaging mode is governed by Rutherford scattering and it is proportional to the thickness of the structure (t) and the atomic number of the material (Z) according to the relationship $I \propto tZ^{\varepsilon}$ where the exponent is in the range of 1.6-2 (related to the detection angle). For the HAADF scattering intensity histogram (Fig. 3k), the frequency of each of the peaks was fitted to a single Gaussian**.**

8. HRTEM Simulations of Bi_2Te_3 nanosheets

Simulations of HRTEM images for Bi_2Te_3 at zero defocus and for a number of z plane/thickness configurations were calculated using the multislice algorithm in Dr Probe software and the atom positions were projected with Vesta software. The results of the simulations for Bi_2Te_3 (001) for a single layer, a bilayer, a trilayer (unit cell) and two trilayers are shown in Supplementary Fig. 5 along with the experimental data. The profiles of the closest distance neighbouring atoms indicate that the experimental data match well with the single layer case. It is noted that contrast irregularities of the atoms across the experimental image can be attributed to the overlaying thin carbon film, however, this does not retract from the fact that different layer configurations should have certain contrast character, as indicated in the simulations.

9. Caption for Supplementary Movie 1

Dissolution and chemical exfoliation of $K_{0.4}MoS_2$. Dry DMF (left) and DI water (right) are added to equal amounts of $K_{0.4}MoS_2$ powder in quartz cells (path length 0.4 mm). The video shows in real time the first ~28 seconds following solvent addition. Whilst no visible chemical reaction occurs upon the addition of aprotic DMF, the water reacts with the $K_{0.4}MoS_2$ evolving hydrogen gas between the layers, exfoliating the sheets to form a dispersion. After 20 days photographs of the same samples are shown. The quartz cells have been rotated 90˚ to view through the longer path length of each cell (1 mm) to highlight the contrast between the samples. Some of the $K_{0.4}MoS_2$ has now dissolved in the aprotic DMF to form a brown/yellow solution, whilst the $K_{0.4}MoS_2$ dispersion in water has mostly flocculated.

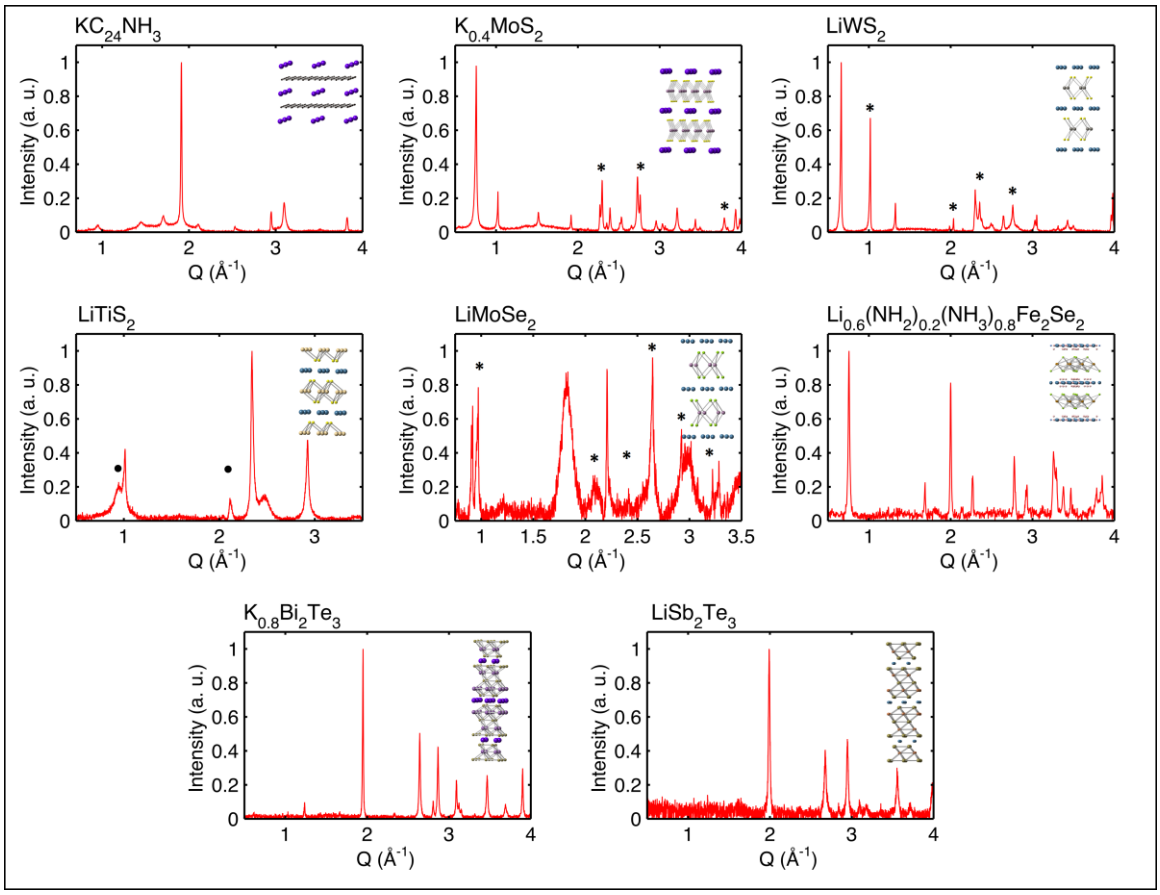

Supplementary Figure 1 | XRD of layered material salts. XRD patterns of the layered material salts and (inset) corresponding structural models. Peaks from remnant non-intercalated layered materials are marked with an asterisk. Unidentified peaks are marked with a filled black circle.

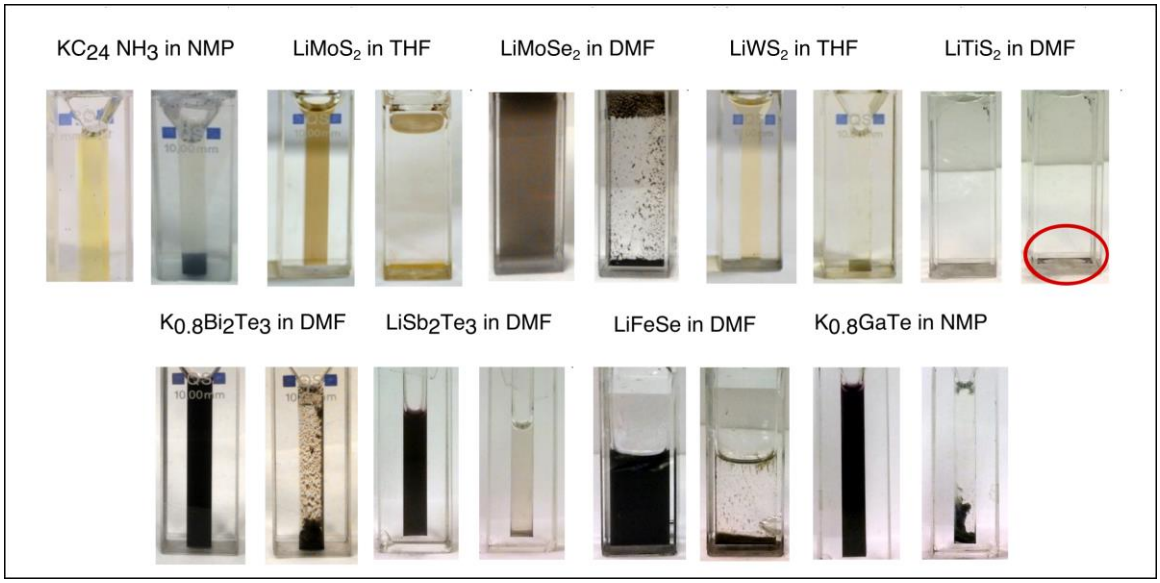

Supplementary Figure 2 | Solutions of layered material salts. Photographs of spontaneously dissolved layered material salts in inert atmosphere (left hand side) and having flocculated following exposure to air (right hand side).

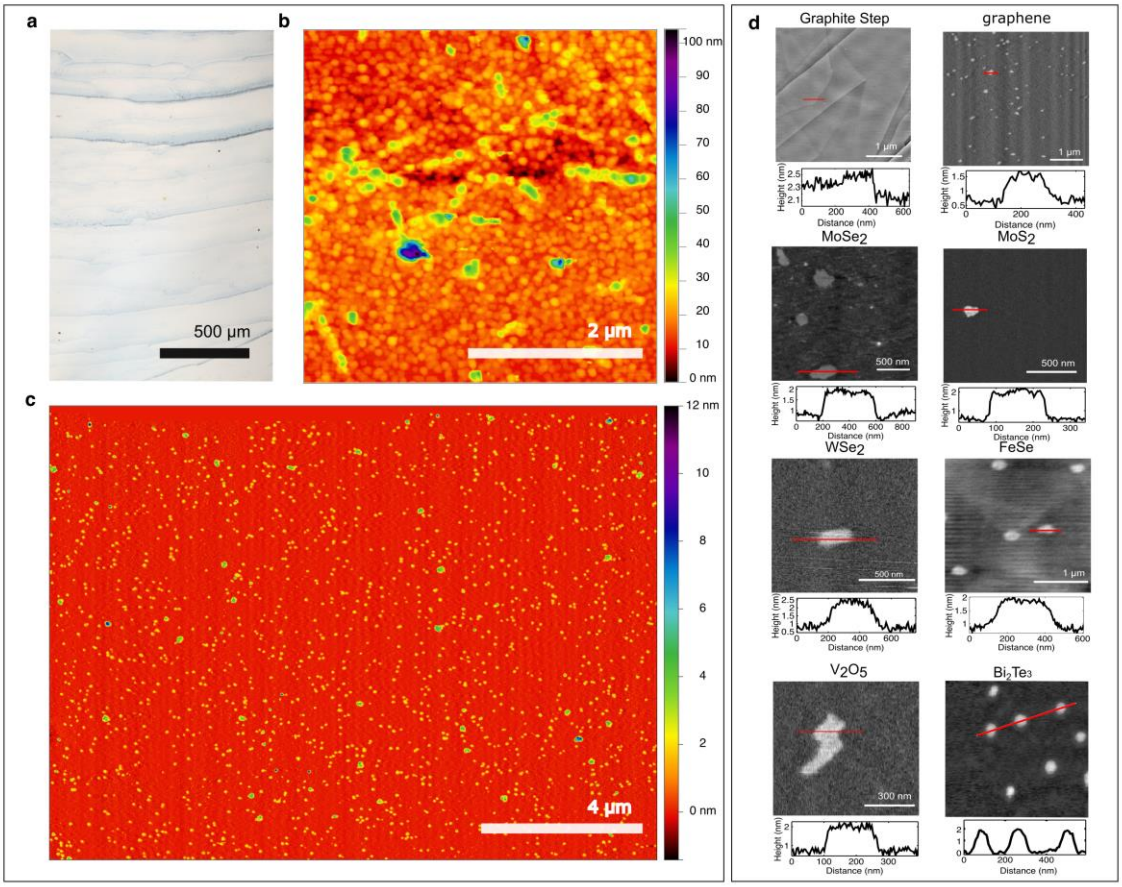

Supplementary Figure 3 | HS-AFM of solution deposited nanosheets. a, Optical micrograph of coffee rings from a $K^+[Bi_2Te_3]^-$/NMP solution dried onto a mica substrate. **b**, HS-AFM taken on a coffee ring from the sample shown in **a**, revealing high concentrations of overlapping Bi_2Te_3 nanosheets, and **c** away from the coffee ring displaying isolated monolayer Bi_2Te_3 nanosheets. **d** Individual HS-AFM frames showing nanosheets deposited from solution for seven layered materials, alongside associated linecuts corresponding to the red lines in the figure. Also shown (top left) is HS-AFM frame from a graphite step used to measure the step height in Fig. 2**f**.

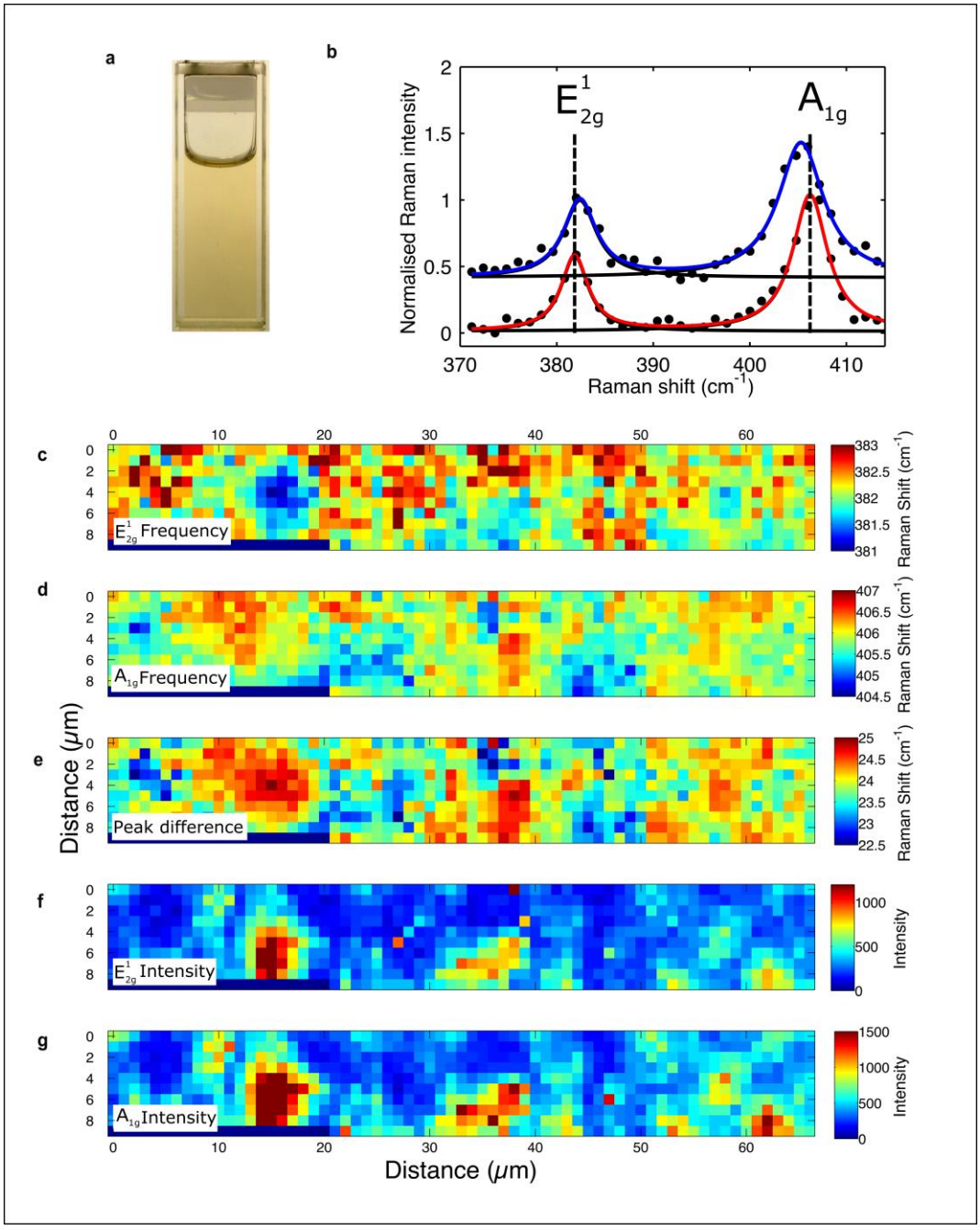

Supplementary Figure 4 | Stability and electroplating of a 2 year old MoS_2 nanosheet solution. a, Photograph of $Li^+[MoS_2]^-$/NMP solution taken 2 years after spontaneous dissolution, showing no signs of solute flocculation. **c-g** Raman maps from a 10 μm x 66 μm continuous MoS_2 thin film, electroplated from solution **a** after 2 years. Each measured spot (pixel) taken at micron intervals, gives distinct 2H-MoS_2 spectra **b**. Maps of fitted peak positions (**c**, **d**) and intensity (**f**, **g**) of characteristic Raman active intra-layer MoS_2 phonons at ~383 cm^{-1} and ~406 cm^{-1} respectively. **e**, Map corresponding to the difference in these peak positions – the smaller the difference the lower the number layers in the film, the 383cm^{-1} peak increases in energy and 406 cm^{-1} decreases in energy with decreasing layer number[59]. 2H-MoS_2 is known to restack following deposition[53,55] however, here the film is thin enough to

reveal areas of restacked 2-3-layer thicknesses. The thickness determined via peak separation **e** directly corresponds to the thickness determined via peak intensity (**f**, **g**) as expected. **b**, example (intensity normalized) spectra from areas of thick (red) and thin (blue) regions. None of the 649 spectra showed any peaks that would be present from the 1T-MoS_2 polymorph. Furthermore, none of the spectra showed any peak width increase from starting bulk MoS_2, which would have indicated an increase in defect concentration. This data demonstrates that after 2 years in solution the nanosheets had remain negatively charged, undamaged and in the 2H-MoS_2 phase.

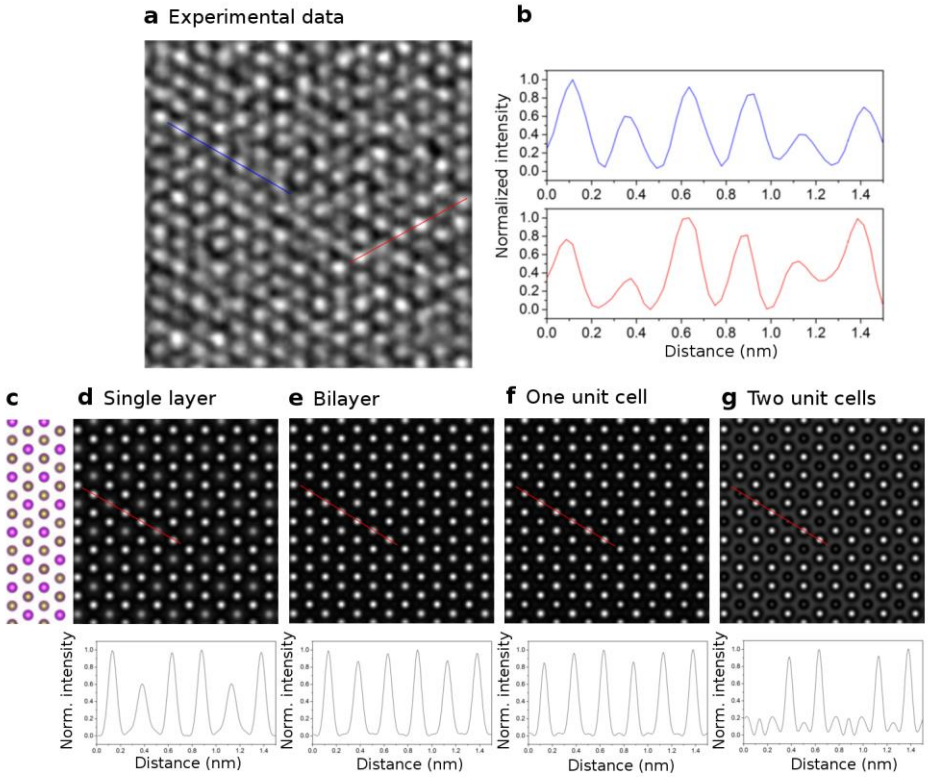

Supplementary Figure 5 | Experimental data and image calculations of high resolution TEM of Bi_2Te_3 (001). a, high resolution electron micrograph of Bi_2Te_3 (001) and **b** profiles across atomic columns indicated in **a**. **d**, **e**, **f** & **g** are image calculations and corresponding profiles of atomic columns **c** for single layer, bilayer, a unit cell and a double unit cell. The contrast of the single layer calculation **d** is the best match of the experimental data despite possible irregularities due to the underlying carbon film.

Supplementary Table 1 | Properties of bulk layered materials used in this work.

Material	Symmetry	Lattice parameters (Å)	Electronic properties	Band gap (eV)	Monolayer unit spacing
Graphite	P63/mmc Hexagonal	a=2.464 c=6.711 [60]	Semi-metal	0	c/2
MoS_2	P63/mmc Hexagonal	a=3.160 c=12.295 [61]	Indirect bandgap semiconductor	1.23 [62]	c/2
$MoSe_2$	P63/mmc Hexagonal	a=3.288 c=12.931 [63]	Indirect bandgap semiconductor	1.09 [62]	c/2
WS_2	P63/mmc Hexagonal	a=3.180 c=12.500 [61]	Indirect bandgap semiconductor	1.35 [62]	c/2
TiS_2	P-3m1 Hexagonal	a=3.4073 c=6.008 [64]	Semi-metal	N/A [62]	c
Bi_2Te_3	R-3m Rhombohedral	a=4.383 c=30.487 [65]	Semiconductor	0.15 [66]	c/3
Sb_2Te_3	R-3m Rhombohedral	a= 4.264 c=30.458 [67]	Semiconductor	0.28 [66]	c/3
FeSe	P4/nmm Tetragonal	a=3.768 c=5.519 [68]	Metal	N/A	c
V_2O_5	Pnm2-1 Orthorhombic	a=11.375 b=4.318 c=3.519 [69]	Direct band gap semiconductor	2.35 [69]	b
GaTe	C 2/m Monoclinic	a=17.404 b=4.077 c=10.456 β=104.44° [70]	Direct gap semiconductor	1.79 [62]	~c

Supplementary Table 2 | Experimental parameters of the intercalated materials

Layered material	Outgassing temperature (°C)	Metals used	Stoichiometry (M : L)
Graphite (powder, Sigma-Aldrich)	400	K	1 : 24
MoS_2 (powder, Sigma-Aldrich)	300	Li, K	0.4 : 1
$MoSe_2$ (powder, Sigma-Aldrich)	150	Li	1 : 1
TiS_2 (powder, Sigma-Aldrich)	300	Li	1 : 1
WS_2 (powder, Sigma-Aldrich)	300	Li	1 : 1
Bi_2Te_3 (powder, Sigma-Aldrich)	200	K	0.8: 1
Sb_2Te_3 (powder, Sigma-Aldrich)	100	Li	1 : 1
FeSe (powder, Alfa Aesar,)	100	Li	1 : 1
V_2O_5 (powder, Sigma-Aldrich)	100	Li	3: 1
GaTe (single crystal, Alfa Aesar)	freshly cleaved	K	0.8 : 1

Supplementary References

[41] E. Zurek, P. P. Edwards, R. A. Hoffmann, molecular perspective on lithium–ammonia solutions. *Angew. Chem. Int. Ed.* **48(44)**, 8198-8232 (2009).
[42] Burrard-Lucas, M. *et al.* Enhancement of the superconducting transition temperature of FeSe by intercalation of a molecular spacer layer. *Nat. Mater.* **12(1)**, 15-19 (2013).
[43] Dresselhaus, M. S. & Dresselhaus, G. Intercalation compounds of graphite. *Advances in Physics* **51**:1, 1-186 (2002).
[44] Zhang, R. *et al.* Superconductivity in potassium-doped metallic polymorphs of MoS_2. *Nano Lett.* ***16***(1) 629–636 (2016).
[45] Somoano, R. B., Hadek, V. & Rembaum, A. Alkali metal intercalates of molybdenum disulfide. *J. Chem. Phys.* **58(2)**, 697-701 (1973).
[46] Ding, Z., Viculis, L., Nakawatase, J. & Kaner, R. B. Intercalation and solution processing of bismuth telluride and bismuth selenide. *Adv. Mater*. 13, 797 (2001).
[47] Whittingham, M. S. Chemistry of intercalation compounds: metal guests in chalcogenide hosts. *Prog. Solid State Chem.* **12(1)**, 41-99 (1978).
[48] Hor Y. S. *et al.* Superconductivity in $Cu_xBi_2Se_3$ and its implications for pairing in the undoped topological insulator. *Phys. Rev. Lett.* **104(5)**, 057001 (2010).
[49] Chen, K. P., Chung, F. R., Wang, M., & Koski, K. J. Dual element intercalation into 2d layered Bi_2Se_3 nanoribbons. *J. Am. Chem. Soc.* **137(16)**, 5431-5437 (2015).
[50] York, B. R. & Solin, S. A. Effect of composition on charge exchange, lattice expansion, and staging in potassium-ammonia graphite intercalation compounds. *Phys. Rev. B* **31(12)**, 8206 (1985).
[51] J. N. Coleman *et al.*, Two-dimensional nanosheets produced by liquid exfoliation of layered materials. *Science* **331**(6017), 568-571 (2011).
[52] Zeng, Z. *et al.* An effective method for the fabrication of few-layer-thick inorganic nanosheets. *Angew. Chem. Int. Ed.* **51(36)**, 9034-9037 (2012)
[53] Zheng, J. *et al*. High yield exfoliation of two-dimensional chalcogenides using sodium napthalenide. *Nat. Commun.* **5** 2995 (2014).
[54] Joensen, P., Frindt, R. F. & Morrison, S. R. Single-layer MoS_2. *Mater. Res. Bull*. **21(4)**, 457-461 (1986).
[55] Eda, G. *et al.* Photoluminescence from chemically exfoliated MoS_2. *Nano Lett.* **11(12)**, 5111-5116 (2011).
[56] Fu, J., Tsai, V., Rainer, K. Ã., Dixson, R. & Vorburger, T. Algorithms for calculating single-atom step heights. *Nanotechnology* **10(4)**, 428 (1999).
[57] Misumi, I. *et al.* Reliability of parameters of associated base straight line in step height samples: Uncertainty evaluation in step height measurements using nanometrological AFM. *Precision engineering* **30(1)**, 13-22, (2006).
[58] Erickson, B.W., Coquoz, S., Adams, J., Burns D. J. & Fantner, G.E. Large-scale analysis of high-speed atomic force microscopy data sets using adaptive image processing, *Beilstein J. Nanotechnol.* **3**, 747-758 (2012).
[59] Lee, C. *et al.* Anomalous lattice vibrations of single- and few-layer MoS2. *ACS nano* **4(5)**, 2695-700 (2010).
[60] Trucano, P. & Chen, R. Structure of graphite by neutron diffraction. *Nature* **258**,136-137 (1975).

[61] Wyckoff, R. G. *Crystal Structures* (Wiley, New York, 1967).
[62] Bucher, E. *Photoelectrochemistry and Photovoltaics of Layered Semiconductors*, edited by Aruchamy, A. (Springer Netherlands, Dordrecht, 1992).
[63] James, P. B. & Lavik, M.T. The crystal structure of MoSe2. *Acta Crystallogr.* **16**, 1183 (1963).
[64] Fang, C. M., de Groot, R. A. & Haas, C. Bulk and surface electronic structure of 1T−TiS_2 and 1T−$TiSe_2$. *Phys. Rev. B* **56,** 4455-4463 (1997).
[65] Francombe, M. H. Structure-cell data and expansion coefficients of bismuth telluride. *B. J. Appl. Phys.* **9**, 415-417 (1958).
[66] Zhang, H. *et al*. Topological insulators in Bi_2Se_3, Bi_2Te_3 and Sb_2Te_3 with a single Dirac cone on the surface. *Nat. Phys.* **5**, 438-442 (2009).
[67] Anderson, T. L. & Krause, H. B. Refinement of the Sb_2Te_3 and Sb_2Te_2Se structures and their relationship to nonstoichiometric $Sb_2Te_{3-y}Se_y$ compounds. *Acta Crystallogr. Sect. B-Struct. Sci.* **30**, 1307-1310 (1974).
[68] Kumar R. S. *et al.* Crystal and electronic structure of FeSe at high pressure and low temperature. *J. Phys. Chem. B* **114**, 12597-12606 (2010).
[69] Chakrabarti A. *et al.* Geometric and electronic study of vanadium pentoxide: a density functional bulk and surface study. *Phys. Rev. B* **59**, 10583-10590 (1999).
[70] Gillian, E. G. & Barron, A. R. Chemical vapour deposition of hexagonal gallium selinide and telluride films from cubane precursons: understanding the envelope of molecular control. *Chem. Mater.* **9**, 3037-3048 (1997).